Influence of a Single Grain Boundary on Domain Wall Motion in Ferroelectrics

*Daniel M. Marincel, Huairuo Zhang, Amit Kumar, Stephen Jesse, Sergei V. Kalinin, W. M. Rainforth, Ian M. Reaney, Clive A. Randall, and Susan Trolier-McKinstry**

Epitaxial tetragonal 425 and 611 nm thick $Pb(Zr_{0.45}Ti_{0.55})O_3$ (PZT) films are deposited by pulsed laser deposition on $SrRuO_3$-coated (100) $SrTiO_3$ 24° tilt angle bicrystal substrates to create a single PZT grain boundary with a well-defined orientation. On either side of the bicrystal boundary, the films show square hysteresis loops and have dielectric permittivities of 456 and 576, with loss tangents of 0.010 and 0.015, respectively. Using piezoresponse force microscopy (PFM), a decrease in the nonlinear piezoelectric response is observed in the vicinity (720–820 nm) of the grain boundary. This region represents the width over which the extrinsic contributions to the piezoelectric response (e.g., those associated with the domain density/configuration and/or the domain wall mobility) are influenced by the presence of the grain boundary. Transmission electron microscope (TEM) images collected near and far from the grain boundary indicate a strong preference for (101)/($\bar{1}$01) type domain walls at the grain boundary, whereas (011)/(0$\bar{1}$1) and (101)/($\bar{1}$01) are observed away from this region. It is proposed that the elastic strain field at the grain boundary interacts with the ferro-electric/elastic domain structure, stabilizing (101)/($\bar{1}$01) rather than (011)/(0$\bar{1}$1) type domain walls, which inhibits domain wall motion under applied field and decreases non-linearity.

1. Introduction

One key open problem in the field of ferroelectrics is the way in which domain walls interact with local pinning centers, and the length scale over which defects influence the response. Point, line, and area defects (and, in principle, any source of local electric or elastic fields) can act as pinning sites for domain wall motion and can lead to nonlinearity coupled with hysteresis in the dielectric and piezoelectric response at sub-switching applied electric fields.[1–6] However, the quantitative influence of specific pinning sites on the measured dielectric and piezoelectric nonlinearities is currently unknown. The approach taken here is to utilize the piezoelectric response [7,8] to study the way in which the nonlinear response develops across a single, well-defined grain boundary.

There are previous reports on the collective influence of grain boundaries on the observed domain structure and domain wall mobility of ferroelectrics. For example, coupling of domain structure across grain boundaries has been observed in TEM images of lead zirconate titanate ceramics[9] and lead titanate thin films[10] as a result of long-range electric and elastic fields. Phase field simulations of domain structures in polycrystalline materials show coupling of domains across grain boundaries[11] with switching in one grain propagating to a neighboring grain.[12] It has also been shown by computational modeling that 90° domain walls prefer not to intersect certain types of grain boundaries, but to have nearly parallel polarization orientations on either side of the grain boundary.[13]

From the standpoint of functional properties, grain boundaries are known to influence the ensemble dielectric and piezoelectric response. Damjanovic and Demartin showed for $BaTiO_3$ ceramics that a decrease in the irreversible contribution to the direct piezoelectric response resulted from a decrease in the grain size,[14] indicating that grain boundaries act to pin domain walls.[15] In polycrystalline PNN-PZT films, a similar decrease was shown in the nonlinear contribution to permittivity with decreasing grain size.[16] Calculations made using first-principles density functional theory also indicate that pinning of domain walls at grain boundaries is energetically favorable.[17] It was further shown experimentally that domain walls do not easily move over grain boundaries at low fields.[18,19]

In addition, phase field models indicate that domains preferentially nucleate at grain boundaries upon back-switching.[11–13] In general, back-switching tends to occur by initial nucleation of 90° domains in one grain to decrease the local electrical

D. M. Marincel, Prof. C. A. Randall,
Prof. Susan Trolier-McKinstry
Department of Materials Science and Engineering
and Materials Research Institute
The Pennsylvania State University
University Park, PA, 16802, USA
E-mail: set1@psu.edu
Dr. H. Zhang, W. M. Rainforth, I. M. Reaney
Department of Materials Science and Engineering
University of Sheffield
Sheffield, S13JD, UK
Dr. A. Kumar, S. Jesse, Dr. S. V. Kalinin
The Center for Nanophase Materials Sciences
Oak Ridge National Laboratory
Oak Ridge, TN, 37831, USA

DOI: 10.1002/adfm.201302457

Table 1. Pulsed Laser Deposition Conditions.

Composition	Pressure [mTorr]	Temperature [°C]	Substrate Distance [cm]	Laser Energy [J cm^{-2}]	Repetition Rate [Hz]	# Pulses
$SrRuO_3$	160	680	8	1.1	10	600
$Pb(Zr,Ti)O_3$	100	630	6	1.2	10	18 000/7800

energy density, followed by propagation into neighboring grains.[12] Local switching by PFM further indicates that domain nucleation may be preferred at grain boundaries.[20] If grain boundaries act only as strong pinning sites, there will be a low irreversible contribution to the piezoelectric and dielectric response near the boundaries due to reduced domain wall motion. However, if domains nucleate at grain boundaries upon back-switching, the concentration of domain walls interacting with weaker pinning sites would increase, leading to an increase in the irreversible contribution to the piezoelectric and dielectric response.

In many cases, the Rayleigh model can be used to describe the nonlinear dielectric and piezoelectric response of ferroelectric materials.[21] In the Rayleigh model, the dielectric and piezoelectric responses are described by a reversible component, d_{init} and $\varepsilon_{\text{init}}$, and an irreversible component, α_d and α_e, which denotes the nonlinear response as a function of magnitude of an applied AC electric field:

$$d = d_{\text{init}} + \alpha_d E_0 \quad (1)$$

$$\varepsilon = \varepsilon_{\text{init}} + \alpha_e E_0 \quad (2)$$

Recent developments of local measurements for piezoelectric response offer the opportunity to follow the evolution of the macroscopic response.[22–25] Characterization of both polycrystalline and epitaxial films demonstrates complex domain structures by band excitation piezoresponse force microscopy revealing clusters of high nonlinear response with sizes larger than the average grain or domain size. Thus, there must be cooperative movement of domain walls across grain boundaries.[7]

One of the consequences of domain wall motion coupling across grain boundaries is that previous studies have sampled multiple pinning centers in their measurements. To better understand the influence of any single pinning site to the response, new data are required which isolate the influence of a single defect on the observed response. Specifically, in this contribution the role of an individual grain boundary is considered.

2. Experimental Procedure

Bicrystal (100) $SrTiO_3$ substrates, 5 mm diameter and 0.5 mm thick, with a tilt angle of 24° (MTI Corp.) were used to engineer a single grain boundary at a known, well-defined angle in a ferroelectric film. Epitaxial $SrRuO_3$ bottom electrodes were deposited on the $SrTiO_3$ substrates by pulsed laser deposition (PLD) using a KrF excimer 248 nm laser (Lambda Physik Compex Pro), as described elsewhere.[26] This was followed by depositing PZT by PLD from a target batched at a Zr/Ti ratio of 45/55 with 20% excess PbO. PZT films were deposited on the bicrystal substrates with multiple thicknesses to determine whether the range of influence of a grain boundary on piezoelectric nonlinear response is thickness dependent. The results reported are for representative samples with thicknesses of 611 nm and 425 nm (Tencor 500 Contact Profilometer). Deposition conditions are provided in **Table 1**.

Photolithography followed by sputter deposition of platinum (Kurt Lesker CMS-18) 10 nm (611 nm thick PZT film) or 50 nm (425 nm thick PZT film) thick was used to define capacitors across the grain boundary so that PFM measurements could be made with a well-defined electric field. Alternating exposure to buffered oxide etchant and HCl was used to etch through the PZT to expose the $SrRuO_3$ bottom electrode, followed by sputter deposition of Pt on the exposed $SrRuO_3$ to improve adhesion for wirebonding to the bottom electrode. Samples were packaged (Spectrum Semiconductor Materials, Inc., CCF04002) on a silicon spacer so that the top of the sample was flush with the top of the package. A Kulicke and Soffa Industries, Inc. wedge wirebonder with gold wire was used to make electrical connections between the sample electrodes and the package.

Electrical measurements of capacitance and dielectric loss (HP 4284A Precision LCR Meter) were made at low field (30 mV, 10 kHz) and as a function of AC voltage up to 50% of the coercive voltage (½V_C) at 300 kHz, near the frequencies used in BE-PFM, to determine the dielectric nonlinearity. Polarization versus voltage measurements were made using a Radiant RT-66 system to assess the ferroelectric hysteresis behavior.

BE-PFM measurements were conducted at the Center for Nanophase Materials Science at Oak Ridge National Laboratory using an Asylum Research Cypher with platinum-coated silicon tips (Nanosensors PPP-EFM-50) as described previously.[7,8,25,27] In this work, the signal was applied to the bottom electrode, while the top electrode and the tip were grounded. Samples were poled at $8V_C$ for 15 min and aged for 30 min prior to measurement. Maps were collected across the grain boundary at a pixel size of 50 or 30 nm and approximately 0.5 mm from the grain boundary at a pixel size of 50 nm.

In order to increase the amplitude of the piezoelectric strain, measurements by BE-PFM were made to 18 kV cm^{-1} (≈0.5 V_C), beyond the electric field associated with the Rayleigh-like regime exhibited by electrical measurements (≈5.2 kV cm^{-1}). Because measurements were made beyond the Rayleigh regime, reported values for nonlinear response are simply the ratio of the quadratic to linear coefficients from the amplitude of response as a function of electric field, in units of cm kV^{-1}, rather than the ratio of the irreversible (α_d) to reversible ($d_{33,\text{init}}$) components from the Rayleigh law. Clustered regions of high and low nonlinear response are evident in all maps, as has

been observed previously.[7,8,25,27] The clusters of high nonlinear response were defined as the regions having nonlinearity above the mean film nonlinearity by more than half a standard deviation, with cluster size off-boundary reported as equivalent circular diameters. A similar analysis was performed to determine regions of low nonlinear response.

Transmission electron microcopy was conducted to observe the domain structure near the grain boundary. It has been reported in PZT that the surface domain configuration may be altered by mechanical grinding.[28,29] Therefore, to avoid domain reorientation during specimen preparation, a dual beam FIB/SEM FEI Quanta 3D 200 machine was employed to prepare transmission electron microscope (TEM) specimens. The grain boundary of the bicrystal was initially located by scanning electron microscopy (SEM), then both cross-section and plan-view TEM specimens containing the grain boundary were prepared by focused ion beam (FIB). A field emission JEOL 2010F TEM/STEM and a JEOL 2010 TEM with Gatan 925 double tilt rotation analytical holder, both operated at 200 kV, were employed for TEM characterization.

3. Results

X-ray diffraction (Philips Pro MRD) showed phase pure PZT in a tetragonal perovskite structure. A phi scan on the PZT 101 peak confirmed epitaxy on both sides of the bicrystal grain boundary. Rocking curves were measured for both samples, with a full width at half maximum of 0.76° in ω for the 611 nm thick film and 0.60° in ω for the 425 nm thick film.

Electrical measurements of the 611 nm thick sample made on electrodes off the grain boundary showed a well-saturated P-E hysteresis loop with remanent polarization of 41.6 μC cm^{-2} and low-field permittivity of 576 with a loss tangent of 0.015. Analysis of the dielectric nonlinearity at 300 kHz after poling showed Rayleigh-like response up to 5.3 kV cm^{-1} with a reversible component of 480.2 ± 0.2 and an irreversible component of 7.16 ± 0.07 cm kV^{-1}, giving an irreversible/reversible ratio of 14.9 ± 0.2 × 10^{-3} cm kV^{-1}. All dielectric Rayleigh parameters are reported in **Table 2**. The 425 nm thick sample showed similar results, with a well-saturated P-E loop with remanent polarization of 41.0 μC cm^{-2} and low-field permittivity of 456 with a loss tangent of 0.010. Analysis of the dielectric nonlinearity at 300 kHz after poling showed Rayleigh-like response up to 5.2 kV cm^{-1} with a reversible component of 428.0 ± 0.2 and an irreversible component of 6.79 ± 0.05 cm kV^{-1}, giving a total irreversible/reversible ratio of 15.9 ± 0.1 × 10^{-3} cm kV^{-1}. Comparison of global measurements made on electrodes containing the boundary to those far from the boundary revealed no variation in Rayleigh character, dielectric loss, or dispersion, leading to the necessity for local measurements.

Table 2. Dielectric Rayleigh Parameters.

Sample Thickness	ε_{init}	α_e [cm kV^{-1}]	$\alpha_e/\varepsilon_{init}$ [10^{-3} cm kV^{-1}]
611 nm	480.2 ± 0.2	7.16 ± 0.07	14.9 ± 0.2
425 nm	428.0 ± 0.2	6.79 ± 0.05	15.9 ± 0.1

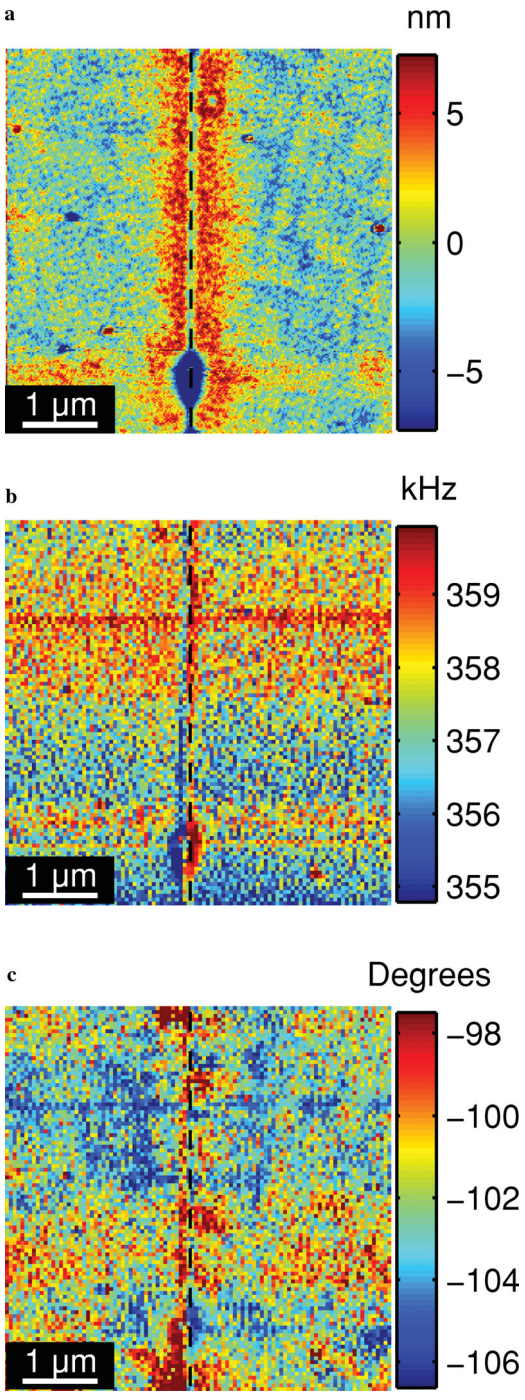

Figure 1. Maps collected on 425 μm thick sample across boundary on the 5 μm × 5 μm region: a) topography, b) resonant frequency, and c) phase of signal at resonance. The dotted line denotes the grain boundary.

Local measurements of the piezoelectric nonlinearity using BE-PFM were made across and far to either side of the boundary. **Figure 1** shows the topography, resonant frequency, and phase collected at each point on the 5 μm × 5 μm region on the 425 nm thick sample. The resonant frequency for each region measured varies at most by 6 kHz at the grain boundary,

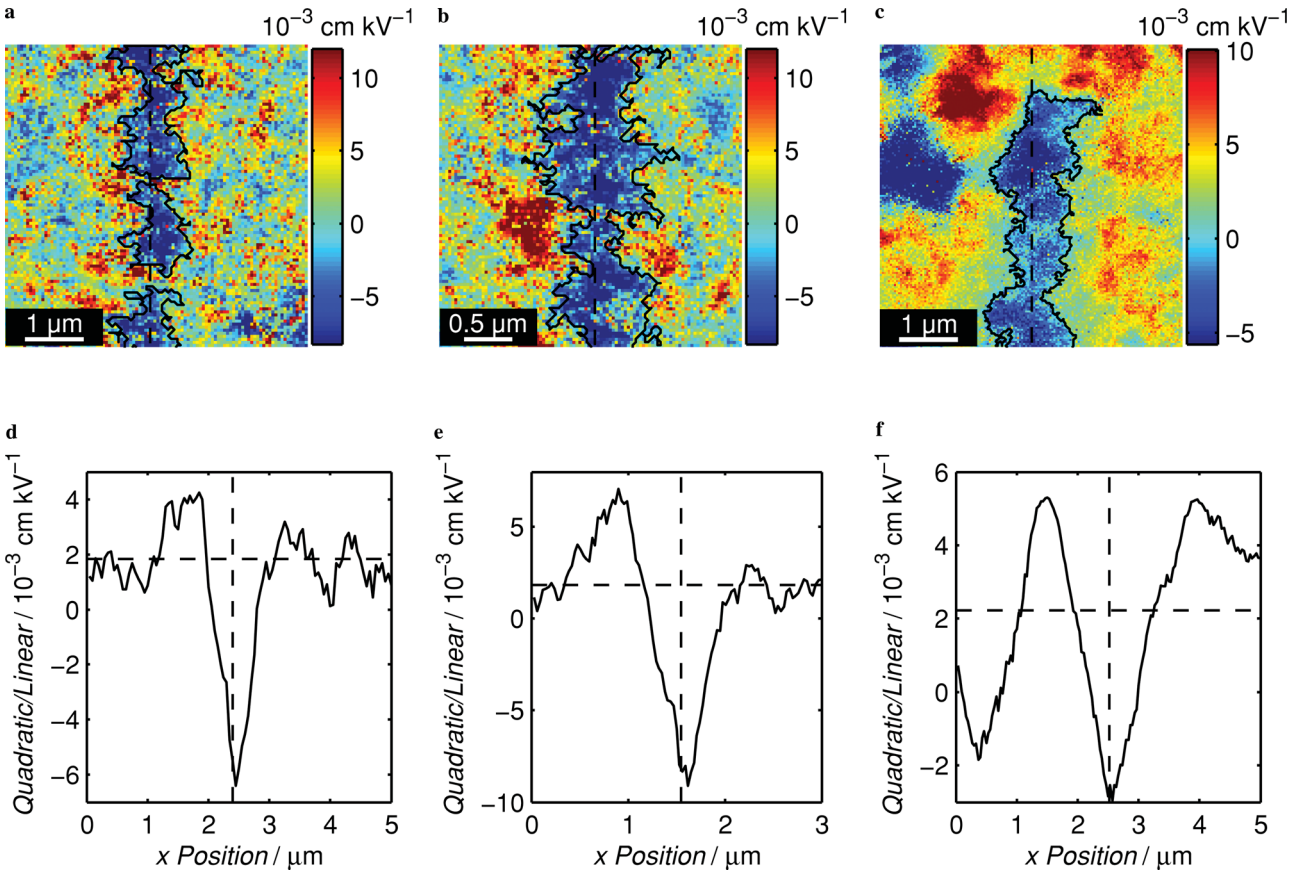

Figure 2. Nonlinear response quadratic/linear maps measured across the grain boundary for the 425 nm thick sample a) 5 μm × 5 μm and b) 3 μm × 3 μm and for the 611 nm thick sample c) 5 μm × 5 μm. Dotted lines denote the location of the grain boundary and solid lines border the selected regions of low response across the boundary for analysis. Plots (d–f) show the nonlinear response quadratic/linear for maps averaged across y positions where (d) corresponds to map (a), (e) corresponds to map (b), and (f) corresponds to map (c). The vertical line denotes the grain boundary and the horizontal line is the off-boundary average nonlinear response.

which is <2% of the resonant frequency. Such a low variation in resonant frequency at the grain boundary indicates that there was no significant topographical contribution to the nonlinearity measurement or variations in elastic properties. The low variation in phase shown in Figure 1c is characteristic of measurements taken after adequate poling.

As a first approach, the data at each location were treated using the Rayleigh formalism. All maps collected across the grain boundary show a significant decrease in the nonlinear response at the boundary as seen in **Figure 2**a–c, demonstrating that the boundary serves as an effective pinning site. The reduced response at the grain boundary had an average width for the 611 nm thick film of 834 ± 67 nm, while the reduced response for the 425 nm thick film is 722 ± 56 nm averaged across the 5 μm map and 755 ± 48 nm averaged across the 3 μm map. The results shown here are representative of observations from many measurements made under various poling conditions, indicating that this observed decrease is consistent for grain boundaries of this type.

The width of reduced response observed for the 425 nm thick film and the 611 nm thick film indicates that the influence of a grain boundary is not determined by the film thickness. In addition, the width of the region influenced by the grain boundary is substantially larger in scale than the cluster size observed on either side of the boundary due to other pinning centers that may influence domain wall motion. Thus, artifacts associated with the variation in top electrode thickness, which should vary similarly far from and at the grain boundary, do not influence the observed length scale of reduced nonlinear response.

Local measurements collected on the 425 nm thick film indicate that there is variation in response from location to location. The mean quadratic to linear ratio varied from the left of the boundary at $0.74 \pm 0.10 \times 10^{-3}$ cm kV^{-1} to the right side of the boundary at $2.95 \pm 0.10 \times 10^{-3}$ cm kV^{-1}. Mean ratios and standard deviations for all maps discussed are included in **Table 3**. This variation is likely due to a greater portion of the nonlinear response becoming negative in the map measured far to the left of the boundary, establishing a tendency toward a non-Rayleigh response. Regions with non-Rayleigh response are expected due to the local piezoelectric measurement being made up to fields beyond the Rayleigh regime. It is significant that regions with both positive and negative quadratic/linear ratios response are still observed. This suggests that the Rayleigh formalism is appropriate in some but not all regions. This may be due to a non-random spatial distribution of pinning sites, a

non-Gaussian distribution of pinning energies, or the presence of interacting domain walls.[30] Using a mean nonlinear response and standard deviation from a combination of the two maps, the region to the left of the grain boundary showed clusters of high (0.23 ± 0.03 μm) and low (0.35 ± 0.11 μm) nonlinear response. The region to the right of the grain boundary showed similar cluster sizes which also exhibited high (0.26 ± 0.05 μm) and low (0.22 ± 0.03 μm) nonlinear response.

The average nonlinear response away from the grain boundary on the 611 nm thick film was measured to be 2.23 ± 0.04 × 10^{-3} cm kV^{-1}. Clusters of high and low response were also observed in this sample with average sizes of 0.23 ± 0.04 μm and 0.24 ± 0.06 μm, respectively, similar to those measured on the 425 nm thick film. It is significant that the region of reduced response observed at the grain boundary on both samples is ≈3 times larger than the high and low response cluster size observed on both samples. This unambiguously demonstrates that the 24° tilt grain boundary influences a larger volume of material than other pinning sites present in these films.

Measurements across the grain boundary were taken on the 611 nm thick film with a 5 μm × 5 μm map at a pixel size of 33 nm. Figure 2c shows the distribution of nonlinearity for the measurement across the grain boundary. The average nonlinearity of the map across the grain boundary is 2.01 ± 0.06 × 10^{-3} cm kV^{-1}, similar to that measured far from the grain boundary. However, the standard deviations are drastically different, at 1.96 × 10^{-3} cm kV^{-1} far from and 4.70 × 10^{-3} cm kV^{-1} across the grain boundary. This large difference was not observed for the 425 nm thick sample, where the standard deviation of the combined maps far from the grain boundary was 5.07 × 10^{-3} cm kV^{-1} and across the grain boundary, 5.31 × 10^{-3} cm kV^{-1} and 6.02 × 10^{-3} cm kV^{-1} for the 5 μm and 3 μm maps respectively. The average nonlinearity of the maps taken across the grain boundary were similar to the average nonlinearity far from the grain boundary with a map average of 1.14 ± 0.10 × 10^{-3} cm kV^{-1} for the 5 μm map and 0.87 ± 0.12 × 10^{-3} cm kV^{-1} for the 3 μm map.

Averaging the nonlinear response parallel to the direction of the grain boundary and plotting as a function of position perpendicular to the boundary as in Figure 2d–f provides information of the average nonlinear response as a function of distance from the grain boundary. The average response is observed to be symmetric with the grain boundary, indicating that the grain boundary pins domain wall motion equally on both sides of the boundary. It is intriguing to note that a maximum in the nonlinear response is observed near the grain boundary immediately neighboring the region of low nonlinearity.

To reveal the fundamental mechanisms of a well-defined grain boundary on the movement of domain walls, comparison of the domain structure near and far from the grain boundary is essential. **Figure 3** is a set of TEM diffraction contrast images obtained near the [100] zone axis, showing the typical domain structures near the grain boundary in an unpoled specimen. Needle shaped domains with (011)/(0$\bar{1}$1) domain walls inclined ≈±45° to the

Table 3. Mean and Standard Deviation of Nonlinear Response Measured by BE-PFM.

Sample Thickness	Region	Mean Quadratic/Linear [10^{-3} cm kV^{-1}]	Standard Deviation [10^{-3} cm kV^{-1}]
611 nm	Off Boundary	2.23 ± 0.04	1.96
611 nm	Across Boundary	2.01 ± 0.06	4.70
425 nm	Left of Boundary	0.74 ± 0.10	4.99
425 nm	Right of Boundary	2.95 ± 0.10	4.89
425 nm	5 μm Across Boundary	1.14 ± 0.10	5.31
425 nm	3 μm Across Boundary	0.87 ± 0.12	6.02

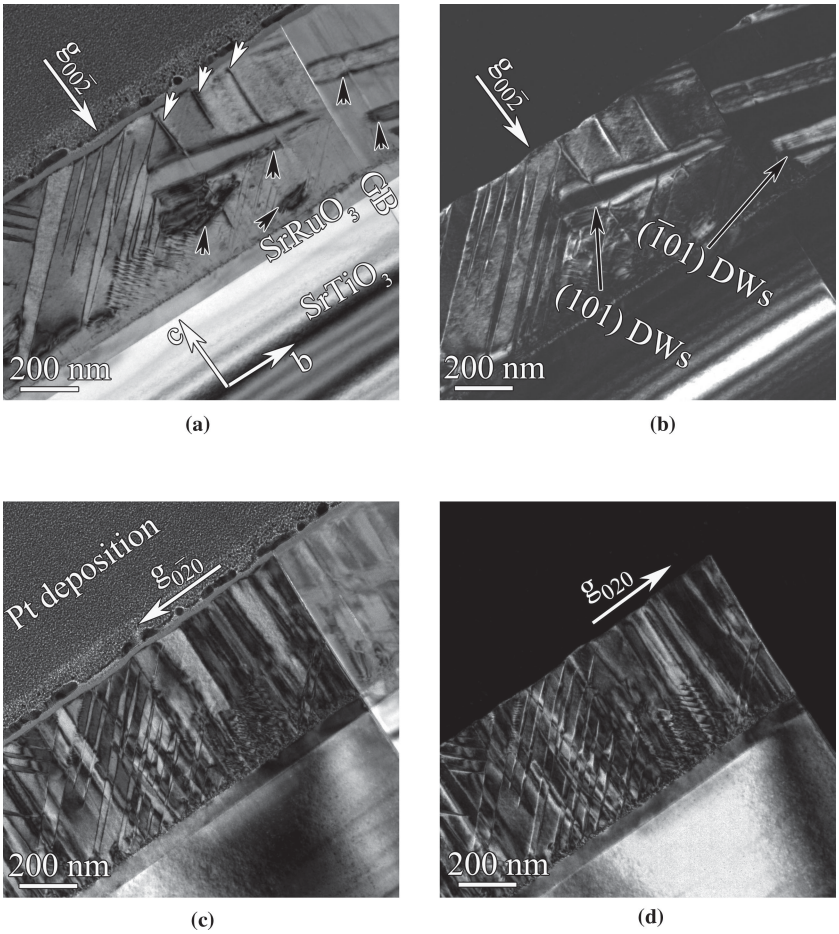

Figure 3. Cross-sectional TEM images of virgin specimen obtained near the [100] zone axis (left grain) showing the domain structures near the grain boundary: a) bright field and b) dark field images with diffraction vector g = 00$\bar{2}$, c) bright field image with g = 0$\bar{2}$0, d) dark field image with g = 020.

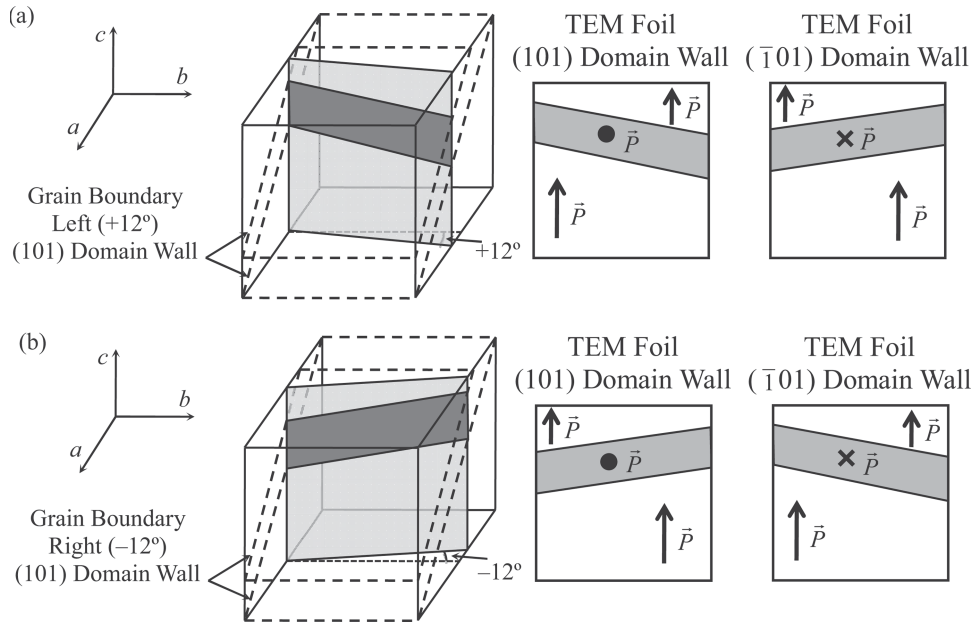

Figure 4. Schematics illustrating how FIB has been used to cut a TEM thin foil specimen (shown in light gray) from a matrix containing (101) domain walls. The schematic illustrates foil specimens with (101) and ($\bar{1}$01) domain walls with the cutting direction: a) clockwise 12° and b) counter-clockwise 12° about the *c*-axis off the (100) plane.

PZT/SRO interface are apparent in the PZT film. For convenience, the coordinate system of the matrix is defined with the *a*-axis nearly parallel to the grain boundary, the *b*-axis nearly perpendicular to the grain boundary, and the *c*-axis perpendicular to the substrate. Therefore, domains are defined as *a*-domain when the polarization vector is along the *a*-axis, as *b*-domain when the polarization vector is along the *b*-axis, and as *c*-domain when the polarization vector is along the *c*-axis of the matrix. The (011)//(0 $\bar{1}$ 1) domain walls observed in Figure 3 separate tetragonal *b*- and *c*-domains, presumably in the non-charged 'head-to-tail' configuration.

However, a different domain structure indicated by black arrows in Figure 3a,b, dominates ≈500 nm on either side of the grain boundary. Figure 3c,d illustrates that the domain walls in the vicinity of the grain boundary are out of contrast when imaging with $\pm g_{020}$ conforming to $g \cdot R = 0$ and defining the habit plane as being within the (h0l) trace. The allowed domain wall habit planes within this trace for tetragonal PZT are (101)//($\bar{1}$ 01), defining *a*-domains alternating with *c*-domains.

The traces of the (101)/($\bar{1}$01) domain walls deviate from the expected orientation parallel to the PZT/SRO interface. This may be explained by considering that cutting the sample in the FIB was carried out perpendicular to the grain boundary, which is rotated ±12° from the (010) plane about the *c*-axis, resulting in domain walls with what initially appeared to be unusual inclination angles within the TEM foil. **Figure 4**a illustrates how the FIB has been used to make a cut 12° clockwise around the *c*-axis from the (100) plane, corresponding to the left side of the grain boundary, with the inclined (101) domain walls retained in the TEM foil. Similarly, a TEM foil with (101) domain walls on the right of the grain boundary (cut counter-clockwise 12°) resulted in inclined domain walls but in opposite orientation, as illustrated in Figure 4b. TEM foils for (101) and ($\bar{1}$01) domain walls on both sides of the grain boundary are also shown. The relative crystallographic planes and orientations of the domains on both sides of the grain boundary can be established according to their trace orientations. The domain walls of the black arrowed domains in Figure 3a,b on each side of the grain boundary are thus determined as (101) and ($\bar{1}$01) for the left and right sides, respectively, with opposite polarization directions within the domains at an angle of 180° – 24° = 156°.

In addition to the cross-hatched domains, a further typical feature of the films is the vertical columnar structure, Figure 3c,d, which is due to threading dislocations, a typical growth defect arising from the lattice mismatch between the PZT and SRO. Most of the threading dislocations are out of contrast when imaging with g_{002}, which suggests that they are primarily edge character dislocations with the Burgers vectors parallel to the PZT/SRO interface. Dislocations with components normal to the PZT/SRO interface are also observed near the grain boundary, as shown by the white arrows in Figure 3a. The strong contrast of the dislocation lines near the grain boundary suggests a pure-screw character with the Burgers vector $\vec{b}$ = [001].[31,32]

Figure 5 shows plan-view images of an unpoled specimen near the grain boundary, obtained along the [001] zone axis. Figure 5a reveals a cross-hatched domain structure typical of a tetragonal ferroelectric phase, where the domain walls are inclined at 45° to the film surface normal. There is a preference near the grain boundary for domains with the major component of the polarization to be parallel to the boundary with *a*- and *c*-domains separated by (101)/($\bar{1}$01) domain walls. These domains are smaller than those observed farther away from the grain boundary and are consistent with the cross-section micrographs. The dark speckles are threading dislocations, which

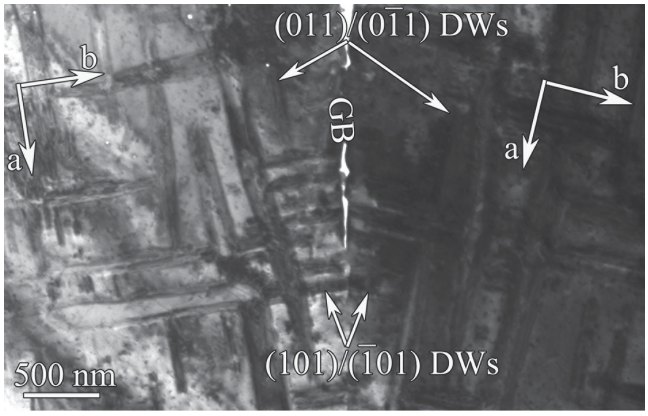

(a)

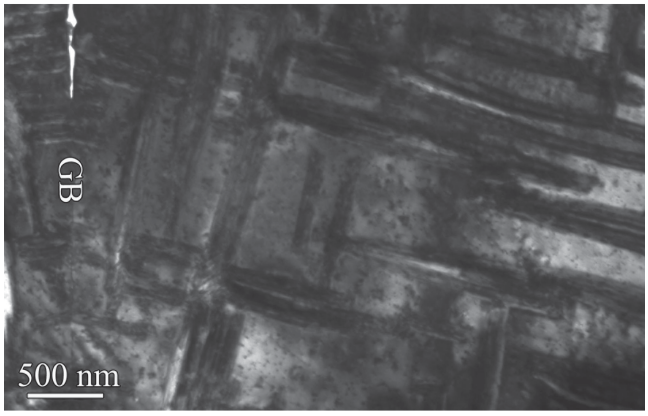

(b)

Figure 5. a,b) Plan-view bright field images of virgin specimen obtained along the [001] zone axis showing the domain structures near the grain boundary.

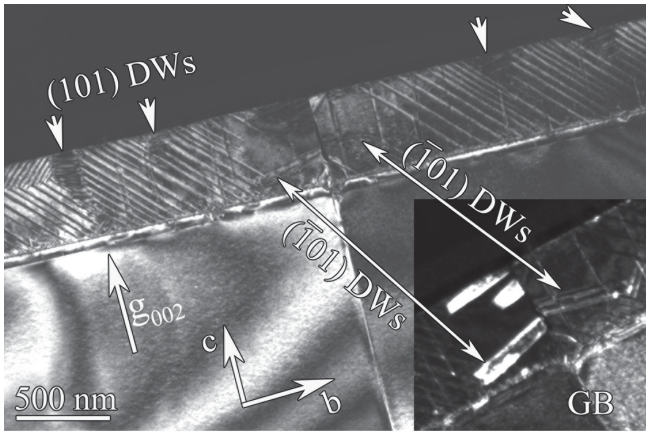

(a)

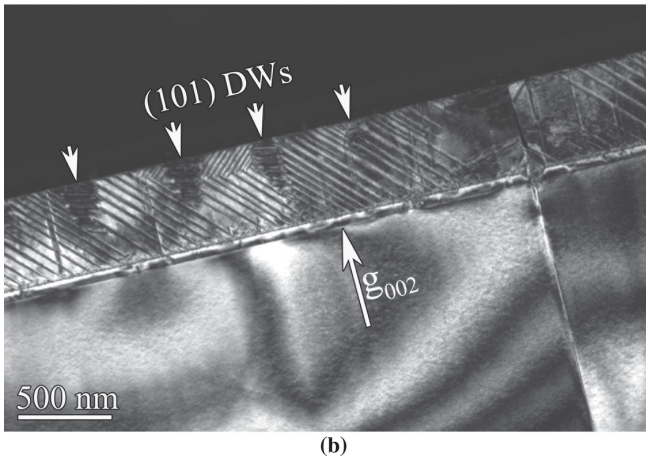

(b)

Figure 6. Cross-sectional TEM images of poled specimen obtained near the [100] zone axis (left grain) showing the domain structures near the grain boundary: a,b) dark field images with diffraction vector g = 002, the inset in the right bottom of (a) obtained in a slight different condition revealing the same ($\bar{1}$01) type domains in both sides of the grain boundary.

have a strain-field around a dislocation core and are visible under certain diffraction contrast conditions.

Figure 6 shows the cross-sectional TEM images of the poled specimen near the grain boundary, obtained near the [100] zone axis. Cross-hatched domain walls are present, with a dense arrangement of *a*-, *b*-, and *c*-domains separated by (011)/(0$\bar{1}$1) and (101)/($\bar{1}$01) domain walls. In Figure 6a,b, (101) type domain walls (shown by short white arrows) appear in the film far away from the grain boundary, but only ($\bar{1}$01) type domain walls appear adjacent to both sides of the grain boundary, as illustrated in the dark field inset in the bottom right of Figure 6a. In contrast to the intersection angle of 156° for the polarization directions of $a^{\text{Left}}/-a^{\text{Right}}$ domains on each side of the grain boundary in the virgin specimen, the intersection angle of $a^{\text{Left}}/a^{\text{Right}}$ domains at the grain boundary in the poled specimen is 24°.

Figure 7 shows the plan-view images of the poled specimen near the grain boundary, obtained along the [001] zone axis. Highly ordered, cross-hatched *a*-, *b*-, and *c*-domains separated by (011)/(0$\bar{1}$1) and (101)/($\bar{1}$01) domain walls are present. Generally, only *a*- and *c*-domains are preferred near the grain boundary, separated by (101)/($\bar{1}$01) type domain walls.

4. Discussion

There are a number of critical observations associated with these results. First, the domain structure observed shows a lower likelihood of (011)/(0$\bar{1}$1) domain walls adjacent to the grain boundary. In order to minimize the strain at the grain boundary, the strain due to the ferroelectric distortion must be the same on both sides of the boundary according to the Fousek-Janovec criteria,[33] which dictates that the deformation of adjacent domains match at their interface. Extending the Fousek-Janovec criteria to consider the permitted domain orientations on either side of a 24° symmetric grain boundary, only *a*- or *b*-domains with an angle of 24° or 156° and *c*-domains with an angle of 0° or 180° between polarization vectors allow the ferroelectric strain on either side of the grain boundary to match.

It is also necessary to examine the intersection of domain walls at the grain boundary. **Figure 8** shows equivalent domain walls from both crystals intersecting the grain boundary. In

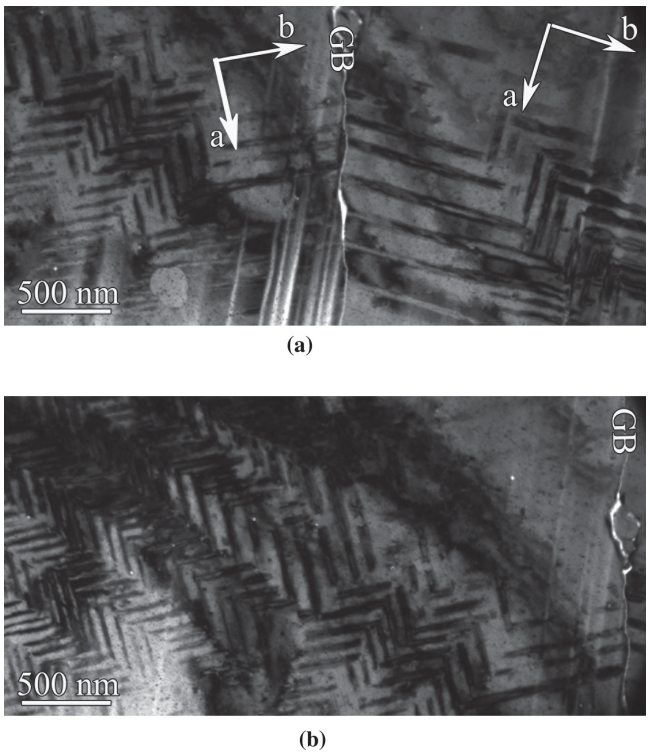

Figure 7. a,b) Plan-view bright field images of poled specimen obtained along the [001] zone axis showing the domain structures near the grain boundary.

Figure 8a, the intersection of (101) domain walls from both crystals lies on the grain boundary, allowing angles between adjacent polarization directions of 24° for *a*-domains and 0° for *c*-domains. Alternatively, Figure 8b shows the intersection of (011) domain walls from both crystals penetrating the grain boundary, requiring adjacent polarizations at the grain boundary with non-allowed angles. This results in additional stress and reduces the likelihood of observing those domain walls.

The manner in which grain boundaries pin domains appears to be related to a change in the domain state influenced by the grain boundary. This is evident from the width of reduced nonlinearity being related to the region with primarily *a*- and *c*-domains in the TEM images. As shown in Figure 6 for the poled domain structure, *b*-domains, with (011)/(0$\bar{1}$1) type domain walls, are not present within 300–500 nm from the grain boundary. This range is consistent with the range of nonlinear response that lies below the film average response, indicating that the (101) as opposed to the (011) domain wall orientation is stabilized at the grain boundary is responsible for the decreased response.

Furthermore, the significant decrease in nonlinear response at the grain boundary in both films indicates that grain boundaries serve as strong pinning centers. The width of the region influenced by the 24° tilt boundaries is large (≈720–820 nm), providing one explanation for observations on both bulk polycrystalline and thin film ferroelectrics on the grain size dependence of the functional properties below ≈1 micrometer grain sizes.[14,15]

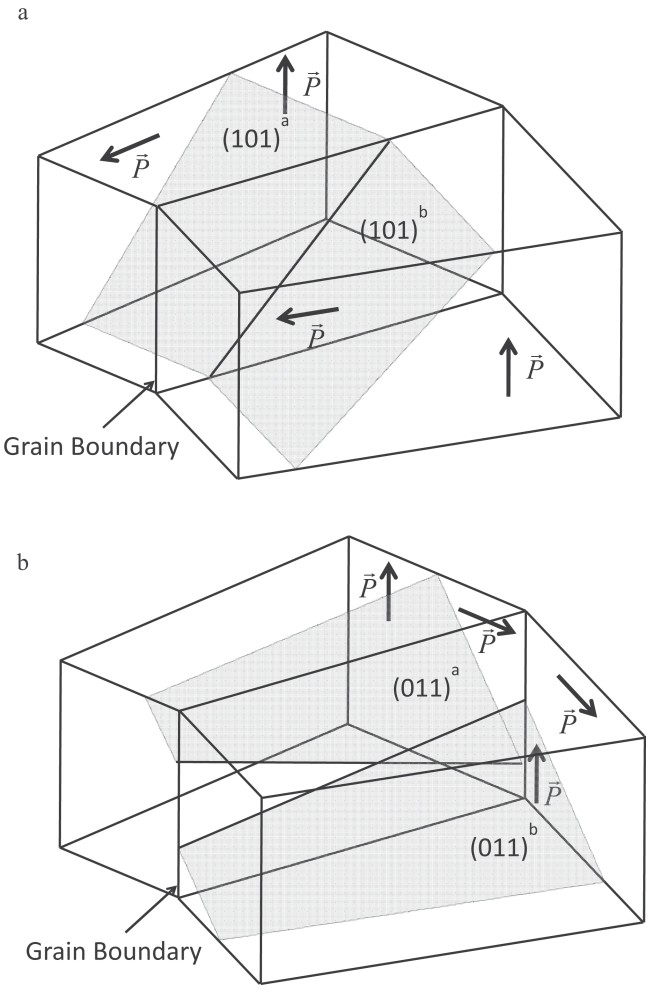

Figure 8. Domain walls from both sides of the grain boundary shown intersecting the grain boundary. a) Intersection between (101) domain walls lies on grain boundary while b) intersection between (011) domain walls does not lie on grain boundary.

It has previously been shown that the nonlinear response in bulk ceramics [1,14] and thin films [27] varies with Zr/Ti content in PZT; a higher nonlinear response is obtained for rhombohedral with respect to tetragonal compositions. Although this has previously been attributed to increased clamping of domain walls due to a larger spontaneous strain in tetragonal compositions, there is also a trend for higher nonlinear response in compositions with a higher density of domain walls. It appears that for the samples examined here the increased concentration of domain walls is likely responsible for the local maxima in the nonlinearity on either side of the grain boundary. Near the grain boundary, there is a preference for *a*- and *c*-domains, as opposed to a mixture of *a*-, *b*-, and *c*-domains farther from the grain boundary. This indicates that near the grain boundary there is a tendency for the polarization to be as close to parallel to the grain boundary as possible. Fewer domain wall variants at the grain boundary may result in a lower nonlinear response due to preferential pinning at the grain boundary. The increase

in possible domain wall variants further from the boundary may result in a higher nonlinear response despite increased domain wall – domain wall interactions under applied field.

5. Conclusions and Summary

A decrease in the piezoelectric nonlinear response was observed at the 24° tilt grain boundary with a total influence of 720–820 nm. A variation in domain structure at the grain boundary was observed with a tendency toward *a*- and *c*-domains with polarization aligned nearly parallel to the grain boundary, whereas *a*-, *b*-, and *c*-domains with (011)/(0$\bar{1}$1) and (101)/($\bar{1}$01) type domain walls are observed farther from the boundary. Through correlation of the TEM and BE-PFM data, the decreased nonlinear response is attributed to this change in the domain wall configurations at the grain boundary, resulting in the grain boundary acting as a strong pinning source for domain wall motion. Regions of high nonlinear response were observed neighboring the minimum at the grain boundary, where *b*-domains with (011)/(0$\bar{1}$1) type domain walls are introduced. Although a symmetric bicrystal was utilized in these measurements, the variation in domain structure observed and its influence on nonlinear response can be applied to multigrain films and ceramics, where the lattice in neighboring grains may not be symmetric across the grain boundary. Large angle tilt grain boundaries result in a change in preferred domain wall orientation near the grain boundary and a decreased nonlinear response, providing an explanation for the properties observed in specimens with sub-micrometer grain size.

Acknowledgements

Support for this work was provided in part by the National Science Foundation Grant No. DMR-10055771 and by CNMS user Proposal No. CNMS2011–022 (DM and STM). H.R.Z., I.R., and W.M.R. would like to acknowledge funding from the Engineering and Physical Sciences Research Council EP/I038934/1. A portion of this research was conducted at the Center for Nanophase Materials Sciences, which is sponsored at Oak Ridge National Laboratory by the Scientific User Facilities Division, Office of Basic Energy Sciences, U.S. Department of Energy.

Received: July 22, 2013
Revised: September 17, 2013
Published online: October 25, 2013

[1] A. Pramanick, D. Damjanovic, J. C. Nino, J. L. Jones, *J. Am. Ceram. Soc.* **2009**, *92*, 2291.
[2] D. V. Taylor, D. Damjanovic, *Appl. Phys. Lett.* **1998**, *73*, 2045.
[3] I. Fujii, M. Ugorek, S. Trolier-McKinstry, *J. Appl. Phys.* **2010**, *107*, 104116.
[4] L. W. Chang, M. McMillen, J. M. Gregg, *Appl. Phys. Lett.* **2009**, *94*, 212905.
[5] P. Gao, C. T. Nelson, J. R. Jokisaari, S.-H. Baek, C. W. Bark, Y. Zhang, E. Wang, D. G. Schlom, C.-B. Eom, X. Pan, *Nat. Commun.* **2011**, *2*, 591.
[6] C. T. Nelson, P. Gao, J. R. Jokisaari, C. Heikes, C. Adamo, A. Melville, S.-H. Baek, C. M. Folkman, B. Winchester, Y. Gu, Y. Liu, K. Zhang, E. Wang, J. Li, L.-Q. Chen, C.-B. Eom, D. G. Schlom, X. Pan, *Science* **2011**, *334*, 968.
[7] P. Bintachitt, S. Jesse, D. Damjanovic, Y. Han, I. M. Reaney, S. Trolier-McKinstry, S. V Kalinin, *Proc. Natl. Acad. Sci. U. S. A.* **2010**, *107*, 7219.
[8] F. Griggio, S. Jesse, A. Kumar, D. M. Marincel, D. S. Tinberg, S. V Kalinin, S. Trolier-McKinstry, *Appl. Phys. Lett.* **2011**, *98*, 212901.
[9] W. Cao, C. A. Randall, *J. Phys. Chem. Solids* **1996**, *57*, 1499.
[10] J. W. Jang, H.-J. Youn, C. Byun, I.-T. Kim, K. S. Hong, *Ferroelectrics* **1999**, *227*, 15.
[11] S. Choudhury, Y. L. Li, C. Krill III, L.-Q. Chen, *Acta Mater.* **2007**, *55*, 1415.
[12] S. Choudhury, Y. Li, C. Krill III, L.-Q. Chen, *Acta Mater.* **2005**, *53*, 5313.
[13] W. Zhang, K. Bhattacharya, *Acta Mater.* **2005**, *53*, 199.
[14] D. Damjanovic, M. Demartin, *J. Phys.: Condensed Matter* **1997**, *9*, 4943.
[15] C. A. Randall, N. Kim, J.-P. Kucera, W. Cao, T. R. Shrout, *J. Am. Ceram. Soc.* **1998**, *81*, 677.
[16] F. Griggio, S. Trolier-McKinstry, *J. Appl. Phys.* **2010**, *107*, 024105.
[17] P. Marton, T. Shimada, T. Kitamura, C. Elsässer, *Phys. Rev. B* **2011**, *83*, 064110.
[18] Y. W. So, D. J. Kim, T. W. Noh, J.-G. Yoon, T. K. Song, *J. Korean Phys. Soc.* **2005**, *46*, 40.
[19] B. D. Huey, R. Nath, S. Lee, N. A. Polomoff, *J. Am. Ceram. Soc.* **2012**, *95*, 1147.
[20] R. Nath, R. E. García, J. E. Blendell, B. D. Huey, *JOM* **2007**, *59*, 17.
[21] D. Damjanovic, M. Demartin, *J. Phys. D: Appl. Phys.* **1996**, *29*, 2057.
[22] S. V. Kalinin, S. Jesse, B. J. Rodriguez, Y. H. Chu, R. Ramesh, E. A. Eliseev, A. N. Morozovska, *Phys. Rev. Lett.* **2008**, *100*, 155703.
[23] V. Nagarajan, S. Aggarwal, A. Gruverman, R. Ramesh, R. Waser, *Appl. Phys. Lett.* **2005**, *86*, 262910.
[24] A. Bernal, A. Tselev, S. V. Kalinin, N. Bassiri-Gharb, *Appl. Phys. Lett.* **2012**, *101*, 112901.
[25] F. Griggio, S. Jesse, A. Kumar, O. Ovchinnikov, H. Kim, T. N. Jackson, D. Damjanovic, S. V. Kalinin, S. Trolier-McKinstry, *Phys. Rev. Lett.* **2012**, *108*, 157604.
[26] D. S. Tinberg, R. L. Johnson-Wilke, D. D. Fong, T. T. Fister, S. K. Streiffer, Y. Han, I. M. Reaney, S. Trolier-McKinstry, *J. Appl. Phys.* **2011**, *109*, 094104.
[27] F. Griggio, S. Jesse, W. Qu, A. Kumar, O. Ovchinnikov, D. S. Tinberg, S. V Kalinin, S. Trolier-McKinstry, *J. Appl. Phys.* **2011**, *110*, 044109.
[28] B. M. Park, S. J. Chung, *J. Am. Ceram. Soc.* **1994**, *77*, 3193.
[29] I. A. Cutter, R. McPherson, *J. Am. Ceram. Soc.* **1972**, *55*, 334.
[30] O. Boser, *J. Appl. Phys.* **1987**, *62*, 1344.
[31] I. B. Misirlioglu, A. L. Vasiliev, S. P. Alpay, M. Aindow, R. Ramesh, *J. Mater. Sci.* **2006**, *41*, 697.
[32] C. J. Lu, L. A. Bendersky, K. Chang, I. Takeuchi, *J. Appl. Phys.* **2003**, *93*, 512.
[33] J. Fousek, V. Janovec, *J. Appl. Phys.* **1969**, *40*, 135.